PAPER

Numerical simulation of the initial stage of unipolar arcing in fusion-relevant conditions

IOP Publishing Plasma Physics and Controlled Fusion
Plasma Phys. Control. Fusion **61** (2019) 095001 (19pp) https://doi.org/10.1088/1361-6587/ab2fac

Numerical simulation of the initial stage of unipolar arcing in fusion-relevant conditions

H T C Kaufmann[1,2], **C Silva**[2] and **M S Benilov**[1,2,3]

[1] Departamento de Física, Faculdade de Ciências Exatas e da Engenharia, Universidade da Madeira, Largo do Município, 9000 Funchal, Portugal
[2] Instituto de Plasmas e Fusão Nuclear, Instituto Superior Técnico, Universidade de Lisboa, 1049-001 Lisboa, Portugal

E-mail: benilov@staff.uma.pt

Received 28 February 2019, revised 24 May 2019
Accepted for publication 4 July 2019
Published 23 July 2019

Abstract

A model for the initial phase of unipolar arcing has been developed with account of an external energy source which triggers the arcing, the vaporization of the atoms from the heated surface, the ions and electrons produced by ionization of the vapor, the electron emission from the metal surface, and melt motion and surface deformation. Current transfer outside the arc attachment is taken into account and the potential difference between the plasma and the metal surface (the plate) is evaluated from the condition that the net current transferred to the plate is zero at each moment. The model is used for simulation of the interaction of an external energy load (laser beam) with a tungsten plate immersed in a helium background plasma. The results revealed the formation of a crater, but no jet formation or droplet detachment. If the plate is large ($R = 100$ mm), the peak temperature attained is 5200 K, and the plate potential remains below the plasma potential. If the plate is small ($R = 10$ mm), a peak temperature of 7500 K is reached, the potential of the plate surpasses the plasma potential, circulation of the melt at the pool periphery occurs, and the erosion (which is mainly due to the vaporization of the metal atoms in the spot) reaches the value of 37 μg.

Keywords: unipolar arcs, plasma-electrode interaction, arc discharges

(Some figures may appear in colour only in the online journal)

1. Introduction

The erosion of the walls, or more specifically, of the plasma-facing components in fusion devices is a possible source of impurities in the core plasma, which may lead to disruptions during the device's operation. Arcing between the plasma and the wall, triggered by so-called edge-localized modes (or ELMs, i.e. plasma instabilities which deliver high energy and particle losses to the plasma-facing components), is thought to be one of the mechanisms of the erosion in devices with high-Z plasma-facing components; e.g. [1–4]. Another possible mechanism of arc triggering is the presence of runaway electrons, which are not only associated with high energy fluxes but also with a large electric field in the sheath region; e.g. [5, 6] and references therein. Since the plasma-facing components are electrically isolated, when an arc is triggered, the current circulates between the plasma and the wall and the net current to the wall is zero: this is the so-called unipolar arc [7].

Arcing in fusion devices is a longstanding research issue; e.g. [5, 8–10] and references therein. Until recently, it was thought that arcing was of minor importance as it is restricted to unstable phases of the plasma operation in fusion devices. However, recently this issue has gained attention (e.g. [1–3] and references therein), in particular due to the decision to begin the operation of the ITER tokamak with a tungsten divertor; e.g. [11] and references therein.

Many dedicated experiments and numerical simulations have been performed to study the behavior of tungsten in response to ELMs and ELM-like transient heat loads, [6, 12–23]. As far as unipolar arcs are concerned, of particular interest is the work [14], which reports a direct experimental observation of a unipolar arc ignited in a stationary plasma. In

[3] Author to whom any correspondence should be addressed.

the experiment, an isolated tungsten plate was exposed to a helium plasma, and then irradiated by a laser pulse, simulating the ELM. The ignition of an arc was evidenced by bright emission detected by a fast camera, an increase of the plate potential from the floating potential, and by erosion trails left on the plate (similar to those observed on tungsten tiles in fusion devices). This line of research has been continued in [19, 24–30]. One of the phenomena observed and studied in these works is the formation of nanostructures on the surface of the tungsten plates due to the background helium plasma irradiation, and it is well understood that the properties of this nanostructure layer are significantly different from those of bulk tungsten [31–34]. The thickness of this layer is a few micrometers, depending on the exposure time to the helium plasma. Arcing was not observed if the laser pulse irradiated the same position twice; this was thought to be due to the destruction of the nanostructures by the energy load delivered by the laser pulse in the first irradiation, which were then absent for the second irradiation [14]. The conclusion was that the nanostructures on the plate surface are essential for arc ignition in the experimental conditions of [14].

With regard to theoretical work, a few papers [25, 27, 30] attempted simulating the behavior of arc spots with modeling based on a phenomenological description of the spot motion; special care was taken to ensure that the model describes grouping of the spots, which occurs in certain conditions and has an effect on the width of the erosion trails left on the plate and on the velocity of overall spot motion. In [33], a numerical analysis of the temperature evolution in the tungsten plate was carried out in an attempt to understand the results of temperature measurements, which showed that melting of the nanostructures had occurred, despite the measured temperature never reaching the melting temperature. As far as the mechanisms responsible for the unipolar arc ignition and sustainment are concerned, it had been proposed [35] that explosions of micrononuniformities on the plate surface due to field emission and Joule heating (the so-called ecton mechanism) would be a key mechanism of both unipolar arcs in fusion devices and cathode spots in vacuum arcs. This line of research was pursued in [28, 36, 37], where the experimental results of [14] and subsequent works were analyzed by means of estimates in the framework of the ecton mechanism.

The results of the above-described experimental works suggest that there are two phases of unipolar arcing. An intense external energy flux, i.e. the laser pulse, causes significant heating of a wide region of the plate surface and the potential difference between the plasma and the plate is reduced by some 30 V; the initial phase. After about 0.6 ms the laser beam is switched off, however the potential difference remains the same and small (much narrower than the laser impact site) bright spots are seen moving away from the impact site. This second phase of unipolar arcing lasts for about 3 ms.

The authors of works [36, 37] assume explosions of the nanostructures, in agreement with the model [35], to be the arcing mechanism of unipolar arcs: a dense plasma existing in the vicinity of a nanostructure causes an intense heating of the structure due to high-density thermo-field electron emission current, which results in an explosion. During the initial phase, the dense plasma is generated, within several microseconds, as the laser radiation is absorbed by the nanostructures and intense vaporization occurs, followed by ionization of the evaporated atoms. During the second phase, a nanostructure is heated by the dense plasma that has been generated at a previous explosion, which occurred in the vicinity.

There is little doubt that explosions of the nanostructures, hypothesized by the authors [36, 37], may be the governing mechanism at the second phase of unipolar arcing. However, this is less certain as far as the initial phase is concerned. Order of magnitude estimates show that, at the laser impact site, a nanostructure with a height of the order of 1 μm, as those of the experiment [14], will be melted within one or few microseconds. Hence, the nanostructures can hardly affect the initial phase of unipolar arcing. A possible alternative mechanism is similar to the mechanism of formation of cathode spots in vacuum arcs: at the heated laser impact site, significant vaporization and electron emission occur, the latter causing the ionization of the emitted vapor. Consequently, current transfer is initiated and the plate potential increases, so that the electron current outside of the impact site compensates the current transfer inside the site, i.e. unipolar arcing is triggered. In this sense, the laser pulse interaction with the surface represents the initial phase of unipolar arcing and the impact site can be called an arc spot. (Note that it appears that the term 'arcing' as used by the authors of [14] refers only to the second phase.)

The formation of cathode spots in vacuum arcs have been modeled in [38–42]: the action of an external energy (and particle) flux ignites a cathode spot, and its subsequent evolution leads to the formation of a crater, and a molten metal jet at the periphery of the crater, and eventually to the ejection of liquid droplets. (It is interesting to note that no microexplosions are reported in virtually all simulation conditions.) It is therefore of interest to apply a similar model for the initial phase of unipolar arcing in fusion devices.

The latter is the objective of this paper. (We stress that modeling of small bright spots that are responsible for current transfer at the second stage of unipolar arcing is beyond the scope of this work.) A model for the initial phase of unipolar arcing in fusion devices is developed on the basis of the detailed numerical model of plasma-cathode interaction in vacuum arcs [40]. The model takes into account an external energy source, which delivers the intense heat flux to trigger the arcing and ignite the arc spot, the vaporization of the atoms from the heated surface, the ions and electrons produced by ionization of the vapor and the electron emission from the metal surface in the arc spot, and relevant hydrodynamic phenomena, including convection and surface deformation. Since the arc is unipolar, the model [40] is supplemented with an account of current transfer outside the arc spot and the potential difference between the plasma and the electrode is evaluated from the condition of the net current to the plate being zero at each moment. The developed model is used for simulation of the interaction of an external energy flux with and current transfer to a tungsten metal plate immersed in a helium background plasma in conditions similar to those of the experiment [14].

The outline of the paper is as follows. The numerical model is introduced in section 2. Results of simulation are reported and discussed in section 3, and a comparison with results of modeling of cathode spots of vacuum arcs is given in section 4. Conclusions are summarized in section 5.

2. The model

The aim of this work is to develop a simulation model of the initial phase of unipolar arcing, i.e. arcing triggered by an intense external energy flux, for conditions related to those which are expected to occur when arcing is triggered in plasma-facing components in fusion devices. Note that the model does not aim at describing the interaction of an ELM with the divertor (or other plasma-facing components) on the whole; rather, a region comprising the arc spot and its surrounding environment is considered in the modeling. The modeling conditions are illustrative of, although not exactly the same as in (see discussion in section 2.3) the experiment [14].

The task of the modeling is to simulate the heating of the laser impact site on the plate surface by an intense external energy flux, the ignition of an arc spot at the impact site due to the initiation of current transfer by electrons emitted and ions produced from the ionization of the emitted vapor at the site, and an increase of the plate potential so that the electron current outside of the arc spot site compensates the current transfer inside the spot. Modeling of small bright spots that are responsible for current transfer at the second stage of unipolar arcing is beyond the scope of this work.

The model employed in this work is based upon a self-consistent detailed numerical model of plasma-cathode interaction in vacuum arcs [40, 43]. The latter models exploit the fact that part of the power deposited into the near-cathode space-charge sheath is transported from the sheath to the cathode surface, while the rest is transported by electric current into the arc column. This means that, to a first approximation, the plasma-cathode interaction is not affected by processes in the arc column. (This approach, which is sometimes called the model of nonlinear surface heating, has been used widely in the theory and modeling of plasma-cathode interaction in arcs in ambient gases, and is quite accurate, despite being the simplest self-consistent approach; e.g. see [44].)

The same approach is used in the model of this work. The thickness of the near-electrode plasma layer is much smaller than the characteristic radius of the arc spot and the spatial distribution of the external energy load, hence current transfer through this layer is locally one-dimensional (1D). The problem of the plasma-electrode interaction may, therefore, be solved in two steps. In the first step, characteristics of the near-electrode plasma layer are evaluated using a 1D model. In particular, the net densities of the energy flux and electric current delivered to the electrode, and the pressure exerted by the plasma over the electrode surface in the arc spot are found. In the second step, distributions of parameters, such as temperature and melt velocity, are calculated in the electrode by means of solving a 2D axially symmetric model.

In other words, the arc plasma is not explicitly considered in the modeling of this work: the parameters of the near-electrode plasma layer evaluated in the first step are introduced as boundary conditions describing the energy and current transfer in the arc spot and pressure acting on the electrode surface in the model of the second step. (This is the same procedure employed in [40, 43].)

A detailed description of the model employed in this work is given in the following sections.

2.1. Equations and boundary conditions

Let us consider a circular metal plate immersed in a background plasma and subjected on one side to an intense external energy load. The model comprises the Navier–Stokes equations describing the motion of the molten metal of the plate, in conjunction with the heat transfer equation in the plate, including both the melt and the solid:

$$\nabla \cdot \mathbf{u} = 0, \tag{1}$$

$$\rho\frac{\partial \mathbf{u}}{\partial t} + \rho(\mathbf{u}\cdot\nabla)\mathbf{u} = \nabla\cdot[-p\mathbf{I} + \mu(\nabla\mathbf{u} + (\nabla\mathbf{u})^T)], \tag{2}$$

$$\rho c_p\frac{\partial T}{\partial t} + \rho c_p\mathbf{u}\cdot\nabla T = \nabla\cdot(\kappa\nabla T). \tag{3}$$

Here ρ is the the mass density of the metal, c_p and κ are the specific heat and the thermal conductivity of the metal, and μ is the viscosity of the melt, $\mathbf{u}$ is the velocity, p is the pressure, and $\mathbf{I}$ is the identity tensor. The equations are solved under the assumption of axial symmetry in cylindrical coordinates (r, z), with material parameters ρ, c_p, κ and μ considered as known functions of the temperature T. The enthalpy-porosity method [45, 46] is used for modeling the solid–liquid phase transition in the metal, which implies solving equations (1) and (2) in the whole of the plate, including both the molten and solid parts (the solution for the velocity vanishes inside the solid part).

Forces due to surface tension effects and due to the pressure p_{pl} exerted by the plasma and by the external energy source are introduced as boundary conditions for the Navier–Stokes equations at the face of the plate subjected to the external energy load, similar to [40]. The pressure p_{pl} comprises contributions from the plasma produced from the metal vapor emitted in the arc spot, p_1, from the background plasma, p_2, and from the external energy load, p_3; the force due to surface tension is evaluated in the usual way, in terms of the curvature of the molten metal surface and the surface tension coefficient of the material. At all the other faces of the plate, the velocity $\mathbf{u}$ is set equal to zero.

The boundary conditions for the heat conduction equation at all the faces of the plate are written in terms of densities of the energy flux q from the plasma to the plate surface. The model takes into account four contributions to q, computed independently of each other:

$$q = q_1 + q_2 + q_3 - q_4, \tag{4}$$

where q_1 is the density of the energy flux to the plate surface due to the vapor emitted in the spot, ions and electrons produced by ionization of the vapor, and the electron emission from the metal surface; q_2 is the density of the energy flux

delivered to the plate by the ions and the electrons from the background plasma; q_3 is the density of the energy flux delivered to the surface by the external energy load, and q_4 is the density of the energy flux lost by the plate surface due to radiation into the plasma. All the above-described terms are taken into account in the boundary condition at the face of the plate which is subjected to the external energy load. q_1 and q_3 are dropped at all the other faces.

Note that it is widely accepted that, as the energy flux from ELMs (or laser beam) significantly heats the plasma-facing components (or metal plate), the evaporation of atoms from the surface will produce a significant amount of vapor that will presumably shield the metal surface from further heating and evaporation due to the external energy load; e.g. see [47, 48]. In order to accurately describe such a phenomenon, a nonlinear interaction between the external energy load and the freshly produced vapor from the arc spot should be considered. The latter is beyond the scope of this work and has not been attempted; instead the simple superposition, equation (4), has been assumed.

The net density of electric current j transferred from the plasma to the metal surface is comprised of two independent contributions,

$$j = j_1 + j_2, \tag{5}$$

where j_1 is the density of electric current due to the ions and electrons generated from the vaporized atoms and due to the emission of electrons in the arc spot; and j_2 is the density of electric current transported to the plate surface by the ions and electrons from the background plasma, which is minor inside the impact area of the external energy load and of primary importance on the rest of the plate surface.

A characteristic of the unipolar arc is that the net current to the plate is zero at every moment. If there is no spot, fluxes of ions and electrons from the background plasma are equal at each point of the plate and the resulting potential of the plate (floating potential) is lower than the potential of the plasma.

When an arc spot is ignited on the plate, the local emission of electrons from the spot reduces the potential difference U between the plasma and the plate from the floating potential to the cathode fall potential of the arc (i.e. the arc burning voltage) [7]; in other words, the potential of the plate increases and approaches that of the plasma. This means that more electrons from the background plasma can cross the sheath and reach the plate against the retarding potential, which has been lowered, thus balancing the current transfer initiated in the arc spot, and satisfying the condition that the total current to the plate is zero at each moment. The variation of the potential difference between the plasma and the plate, $U = U(t)$, is computed with this condition, i.e. the current transferred by the plasma produced in the arc spot I_1 is balanced by the current transferred by the background plasma over the whole surface of the plate. Since j_2 takes the same value at all points of the plate surface, this condition reads

$$I_1 = j_2\, A_{\text{plate}}, \quad I_1 = \int j_1 \, \mathrm{d}A, \tag{6}$$

where the integral is evaluated over the face subjected to the external energy load and A_{plate} is the total surface area of all faces of the plate.

One needs to analyze the distribution of potential at the edge of the near-electrode plasma layer in order to specify a distribution of U along the plate. If the magnetic field were absent, the variation of the potential at the edge in the radial direction could be estimated as $\Delta U = I_1/2\pi r_s \sigma$, where r_s is a characteristic spot radius and σ is the classical conductivity of the background (helium) plasma. Assuming $I_1 = 100$ A, $r_s = 0.5$ mm, and $\sigma = 10^4$ S m^{-1} as illustrative values for conditions of the experiment [14], one finds $\Delta U \approx 3$ V. Neglecting this value compared to characteristic values of U (30–60 V), one can assume U to be the same at each point of the plate. However, this reasoning is changed by the presence of the magnetic field. The analysis performed in [49] has shown that in the case where the magnetic field is perpendicular to the plate, the transverse scale of the return current region is determined by the perpendicular ion viscosity (classical or anomalous) and the longitudinal scale depends on the classical conductivity. In the experiments [14], the magnetic field was 0.1 T and parallel to the plate or oblique. It was found that the inclination angle of the magnetic field affects the motion of the bright spots at the second phase of the unipolar arcing; no effect on the initial stage was reported. In this work, the effect of the magnetic field over the distribution of potential at the edge of the near-electrode plasma layer is not considered and U is assumed to be the same at each point of the plate, i.e. the potential difference between the plasma and the plate is constant over the whole plate.

Furthermore, it should be considered that as the local emission of electrons from the arc spot increases and results in a further reduction of the potential difference between the plasma and the plate, this may lead to an inversion of U; more specifically, the plate potential increases and approaches the plasma potential and may then surpass it, i.e. a transition to a regime where the plate potential is above the plasma potential occurs. This transition is taken into account in the modeling, as described in detail in section 2.2. It is important to note that, independently of the regime (i.e. of whether the plate potential is below or above the plasma potential), the heated area of the plate where the arc spot is ignited operates as a cathode at every moment, while the rest of the plate outside the arc spot always operates as an anode; in other words, the current enters the plate in the arc spot and returns to the plasma from the rest of the plate's surface.

Estimates based on the laser beam characteristics and of plasma parameters in typical experimental conditions show that the pressures exerted on the metal plate by the background plasma, p_2, and by the external energy load, p_3, are negligible when compared to the pressure p_1 exerted by the plasma produced from the metal vapor. Therefore, the pressures p_2 and p_3 are neglected, and $p_{pl} = p_1$.

The initial condition is $T = T_0$ at $t = 0$, where T_0 is the temperature of the plate while it is immersed in the background plasma before the irradiation by the external energy source. T_0 is governed by the condition of equilibrium between the density of the energy flux q_2 delivered by the

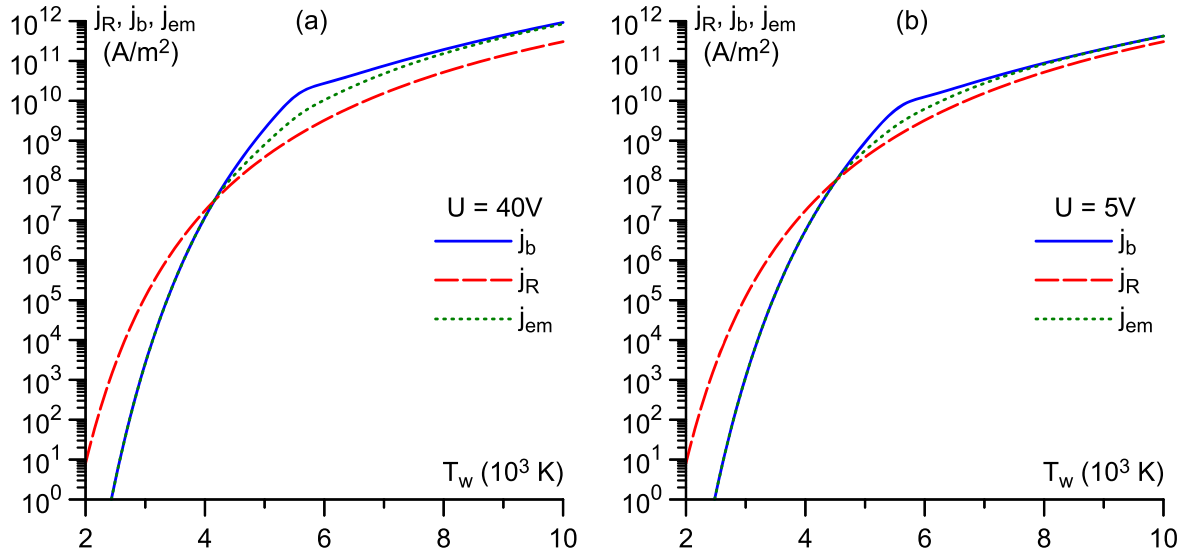

Figure 1. Computed values of j_b, j_R, and j_{em} for two values of the potential difference U between the plasma and the plate, in the range of surface temperatures T_w relevant to the simulations of this work.

background plasma to the plate surface and the density of energy flux q_4 lost by the plate surface due to radiation into the plasma, i.e. $q_2 = q_4$.

The problem is solved numerically by means of the finite-element method. The account of the latent heat of melting is introduced along the same lines as is done in simulation of metal casting [50]. A front-tracking method is implemented for explicitly tracking the deformation of the molten surface on a moving grid.

2.2. Plasma-metal interaction

The choice of conditions of modeling reported in this work is based on the experiment [14]. Let us consider a tungsten (W) plate immersed in a helium (He) background plasma and subjected on one side to an intense energy flux from a laser. We remind, once again, that the initial phase of unipolar arcing is characterized by the interaction of the external energy flux (laser beam) with the metal plate, resulting in the ignition of an arc spot, and the arc spot comprises the laser impact area; see section 1.

The density of electric current j_1 transferred in the arc spot is defined as a function of the local surface temperature T_w and of the potential difference U between the surrounding plasma and the plate, and is given by:

$$j_1 = j_i^{(W)} + j_{em} - j_e^{(W)}, \tag{7}$$

where $j_i^{(W)}$ is the density of current of ions coming to the plate surface, generated from the vaporized tungsten atoms; j_{em} is the electron emission current density; and $j_e^{(W)}$ is the density of current of thermalized electrons of the tungsten plasma that reach the surface of the plate after having overcome the potential barrier.

Quantity j_2 is determined as

$$j_2 = j_i^{(He)} - j_e^{(He)}, \tag{8}$$

where $j_i^{(He)}$ and $j_e^{(He)}$ represent the densities of electric currents of ions and electrons coming to the plate from the helium background plasma.

Let us first consider the regime where the plate potential is below the plasma potential, so $U > 0$. The density of current of ions $j_i^{(W)}$ coming to the plate surface from the tungsten plasma produced in the arc spot is evaluated assuming that all the vapor emitted from the surface is ionized and that all the tungsten ions produced, which are assumed to be singly ionized, return to the surface:

$$j_i^{(W)} = eJ_v. \tag{9}$$

Here e is the electron charge and J_v is the flux of atoms emitted by the plate surface, which is evaluated by means of the Langmuir formula

$$J_v = p_v \Big/ \sqrt{2\pi m_i^{(W)} k T_w}, \tag{10}$$

where p_v is the pressure of the saturated vapor of tungsten, k is the Boltzmann constant, and $m_i^{(W)}$ is the mass of the ions formed from the tungsten metal vapor.

The emission current density j_{em} is evaluated by means of the Richardson–Dushmann formula, with account of the Schottky correction. The surface electric field is obtained by means of the model [51]. The latter takes into account the limitation of the electron emission current by the negative space charge accumulated in the near-electrode layer. In other words, the positive ion space charge of the near-electrode space-charge sheath is partially neutralized by the electrons being emitted in the arc spot; since tungsten is a refractory metal the amount of thermionically emitted electrons present in the sheath is significant and the current density of the emitted electrons has an upper limit, which in the model [51] corresponds to the case of zero surface electric field. As an example, the computed maximum value of the thermionic-emission current density, j_b, is shown in figure 1 for two values of the potential difference between the surrounding plasma and the plate of $U = 40$ V and $U = 5$ V in the range

of surface temperatures T_w relevant to the simulations of this work; the electron temperature $T_e^{(\mathrm{W})}$ of the tungsten plasma is assumed to be 2 eV and the work function A_f is set to 4.55 eV. j_b is strongly dependent on the surface temperature as can be expected, and only weakly dependent on the potential difference. Also shown in figure 1 is the thermionic electron emission current density j_R resulting from the evaluation of the Richardson formula (without the Schottky correction); the Richardson constant for tungsten was assumed to be equal to 60×10^4 A m^{-2} K^{-2} [52]. For T_w below a certain value which depends on U but is generally around 4000 K, $j_\mathrm{R} > j_b$, the surface electric field is zero and the resulting current density j_em coincides with j_b. As T_w increases, both j_R and j_b increase, but j_b increases faster. (This is a consequence of the vaporization energy A_v, which is 7.98 eV for tungsten, exceeding the work function; a feature characteristic of refractory metals.) For temperatures above 4000 K, the situation reverses, i.e. the inequality $j_\mathrm{R} < j_b$ holds, and j_em is given by the Richardson–Dushmann formula (with the Schottky correction) and lies between j_R and j_b.

The density of electric current of thermalized plasma electrons coming to the plate from the tungsten plasma, $j_e^{(\mathrm{W})}$, is evaluated by means of the usual expression

$$j_e^{(\mathrm{W})} = \frac{1}{4} e n^{(\mathrm{W})} \sqrt{\frac{8kT_e^{(\mathrm{W})}}{\pi m_e}} \exp\left(-\frac{eU}{kT_e^{(\mathrm{W})}}\right), \tag{11}$$

where m_e is the mass of an electron and $n^{(\mathrm{W})}$ is the density of the tungsten plasma at the sheath edge. Note that the product of the first to third multipliers on the rhs is the thermal flux of electrons and the last (exponential) factor takes into account reflection of the electrons by the potential barrier. The plasma density is evaluated in terms of $j_i^{(\mathrm{W})}$ and the Bohm speed $\sqrt{kT_e^{(\mathrm{W})}/m_i^{(\mathrm{W})}}$:

$$n^{(\mathrm{W})} = \frac{j_i^{(\mathrm{W})}}{e} \Big/ \sqrt{kT_e^{(\mathrm{W})}/m_i^{(\mathrm{W})}}. \tag{12}$$

The density of the energy flux q_1 coming to the plate surface due to the tungsten vapor emitted in the arc spot, ions and electrons produced by ionization of the vapor, and the electron emission from the metal surface is evaluated as a function of T_w and U, given by:

$$q_1 = q_i^{(\mathrm{W})} - q_\mathrm{em} - q_\mathrm{ev} + q_e^{(\mathrm{W})}, \tag{13}$$

where $q_i^{(\mathrm{W})}$ is the density of the energy flux delivered to the metal surface by incident ions (generated from the vaporized tungsten atoms); q_em and q_ev are the densities of the energy fluxes removed from the surface due to electron emission and vaporization, respectively; $q_e^{(\mathrm{W})}$ is the density of the energy flux delivered to the surface by plasma electrons. These quantities are evaluated as

$$q_i^{(\mathrm{W})} = \frac{j_i^{(\mathrm{W})}}{e}\left(\frac{kT_e^{(\mathrm{W})}}{2} + eU + A_i - A_f\right), \tag{14}$$

$$q_\mathrm{em} = \frac{j_\mathrm{em}}{e}(2kT_w + A_f), \tag{15}$$

$$q_\mathrm{ev} = J_v(A_v + 2kT_w), \tag{16}$$

$$q_e^{(\mathrm{W})} = \frac{j_e^{(\mathrm{W})}}{e}(2kT_e^{(\mathrm{W})} + A_f), \tag{17}$$

where A_i is the ionization energy of tungsten. Note that the term $2kT_w$ on the rhs of equations (15) and (16) describes the average kinetic energy of an emitted electron or vaporized atom leaving the electrode surface. (Both emitted electrons and vaporized atoms are assumed to have a half-Maxwellian distribution; $2kT_w$ appears instead of $\frac{3}{2}kT_w$ because of the difference between the average value of the product of the kinetic energy of motion of the particles and the particle velocity, on one hand, and the product of the average values, on the other.)

The pressure p_1 exerted by the plasma produced from the ionization of the emitted tungsten vapor is evaluated, as a function of T_w and U, by means of expression:

$$p_1 = \frac{2q_i^{(\mathrm{W})}}{\sqrt{2eU/m_i^{(\mathrm{W})}}}. \tag{18}$$

Note that the quantity $\sqrt{2eU/m_i^{(\mathrm{W})}}$ has the meaning of speed of the ions impinging on the metal surface estimated neglecting the kinetic energy of the ions at the sheath edge.

The densities of electric currents of ions and electrons coming to the plate from the helium background plasma, $j_i^{(\mathrm{He})}$ and $j_e^{(\mathrm{He})}$, in the regime where the plate potential is below the plasma potential are evaluated as

$$j_i^{(\mathrm{He})} = eZn_i \sqrt{\frac{kT_i^{(\mathrm{He})} + ZkT_e^{(\mathrm{He})}}{m_i^{(\mathrm{He})}}},$$
$$j_e^{(\mathrm{He})} = \frac{1}{4} e n_e \sqrt{\frac{8kT_e^{(\mathrm{He})}}{\pi m_e}} \exp\left(-\frac{eU}{kT_e^{(\mathrm{He})}}\right). \tag{19}$$

Here n_i, n_e and Z are the ion and electron densities and the ion charge number in the helium background plasma (known parameters; note that $n_e = Zn_i$), $T_e^{(\mathrm{He})}$ and $T_i^{(\mathrm{He})}$ are the electron and ion temperatures of the background plasma, and $m_i^{(\mathrm{He})}$ is the mass of an ion of the helium plasma. Note that the physical meaning of equations (19) is similar to that of equations (12) and (11).

The density of the energy flux q_2 delivered to the plate by the ions and the electrons from the helium background plasma is specified as in [53], with some minor terms (those proportional to the electron emission current density and the Schottky correction) omitted:

$$q_2 = \frac{j_i^{(\mathrm{He})}}{eZ}\left(2kT_i^{(\mathrm{He})} + \frac{ZkT_e^{(\mathrm{He})}}{2} + ZeU + E - ZA_f\right) + \frac{j_e^{(\mathrm{He})}}{e}(2kT_e^{(\mathrm{He})} + A_f), \tag{20}$$

where E is the ionization energy of helium.

Let us now consider the regime where the plate potential is above the plasma potential, corresponding to negative values of the potential difference U between the surrounding plasma and the plate. There is no acceleration of the emitted electrons in the space-charge sheath in this regime and therefore no production of ions or electrons in the

near-electrode region. Therefore, in this regime the terms $j_i^{(W)}$ and $j_e^{(W)}$ in equation (7), the terms $q_i^{(W)}$ and $q_e^{(W)}$ in equation (13) and equation (18) are dropped. The density of electron emission current j_{em} is evaluated by the Richardson formula (without the Schottky correction) with account of the reflection of the emitted electrons by the potential barrier; i.e. equation (7) is written in the form

$$j_1 = j_R \exp\left(\frac{eU}{kT_w}\right). \tag{21}$$

Equations (19) in the regime where the plate potential is above the plasma potential 'exchange places':

$$j_i^{(He)} = \frac{1}{4} eZn_i \sqrt{\frac{8kT_i^{(He)}}{\pi m_i^{(He)}}} \exp\left(\frac{ZeU}{kT_i^{(He)}}\right),$$
$$j_e^{(He)} = en_e \sqrt{\frac{kT_i^{(He)}/Z + kT_e^{(He)}}{m_e}}, \tag{22}$$

and equation (20) is written as

$$q_2 = \frac{j_i^{(He)}}{eZ}(2kT_i^{(He)} + E - ZA_f) + \frac{j_e^{(He)}}{e}\left(2kT_e^{(He)} + \frac{kT_i^{(He)}}{2Z} + A_f - eU\right). \tag{23}$$

Note that the expression for the electron Bohm speed (the last multiplier on the rhs in the second expression of equation (22)) is a general form of the expression derived in [54].

The above assumption that all vaporized atoms are ionized and return to the surface, made for the evaluation of j_1, q_1, and p_1 in the regime where the plate potential is below the plasma potential ($U > 0$), is justified when the energy available for the ionization, W_{avail}, is greater than or equal to the energy required for the ionization of all the vapor emitted. The energy necessary for the ionization of the emitted vapor is $W_{ion} = J_v A_i$. The energy available in the near-electrode plasma layer for the ionization of the emitted atoms may be roughly estimated as

$$W_{avail} = \frac{j_{em}}{e}\left(2kT_w + eU - \frac{5}{2}kT_e^{(W)}\right). \tag{24}$$

Note that the term $2kT_w$ represents the energy of the emitted electrons, eU represents the energy gained by the emitted electrons as they are accelerated in the sheath, and $\frac{5}{2}kT_e^{(W)}$ describes the energy carried away by the electron current leaving the sheath for the bulk plasma, accounting for enthalpy transport.

Numerical estimates show that the condition $W_{avail} \geqslant W_{ion}$ is satisfied for U exceeding approximately 5 V. For lower values of U, W_{avail} becomes smaller than W_{ion} and then very rapidly turns negative, meaning that there is no production of ions or electrons in the near-electrode region. The implication is that an intermediate regime exists in the range $5\,\text{V} \gtrsim U > 0\,\text{V}$, where the transition of the plate potential from below to above the plasma potential occurs. A more careful study is needed in this range. In this work, such a study is not undertaken. Instead, in the range $5\,\text{V} > U > 0$ the terms $j_i^{(W)}$ and $j_e^{(W)}$ in equation (7) and the terms $q_i^{(W)}$ and $q_e^{(W)}$ in equations (13) and (18) are dropped and a linear interpolation is used to smooth the transition from equation (7) at $U = 5\,\text{V}$ to equation (21) at $U = 0$. Equations (7)–(18) are used in the range $U \geqslant 5\,\text{V}$ and equations (19) and (20) in the whole range $U \geqslant 0$.

The density of the energy flux q_3 delivered to the surface by the external energy source (laser beam) is specified as

$$q_3 = q_{peak} f_r(r) f_t(t). \tag{25}$$

Here q_{peak} is a given parameter characterizing the maximum density of energy flux delivered by the external energy source; and $f_r(r)$ and $f_t(t)$ are functions characterizing the spatial distribution and temporal variation of the external energy load and assumed in the form

$$f_r(r) = \exp\left[-\left(\frac{r}{a}\right)^2\right], \quad f_t(t) = \exp\left[-\left(\frac{t - t_0}{\tau}\right)^2\right], \tag{26}$$

where a, τ, and t_0 are given parameters.

The density of the energy flux q_4 lost by the plate surface due to radiation into the plasma is

$$q_4 = \varepsilon\sigma T_w^4, \tag{27}$$

where σ is the Stefan–Boltzmann constant and ε is the emissivity of the tungsten plate surface.

2.3. Material functions

The model of this work does not take into account the nanostructure layer, since the nanostructures within the impact site of the external energy load (i.e. within the arc spot) are rapidly destroyed and will have no effect on the initial phase of unipolar arcing, as evidenced by the estimates given in section 1 and by special simulations reported in section 3.3. Thus, the (temperature-dependent) mass density, specific heat, thermal conductivity, viscosity and surface tension coefficient are set equal to those of bulk tungsten and taken from [55]. The emissivity ε of tungsten is taken from [56]. The pressure p_v of the saturated tungsten vapor is taken from [57–59].

In the experiment [14], the plate potential increases by approximately 30 V from the floating potential in response to the laser irradiation. Assuming 10 V as a typical value of the near-electrode voltage drop during arcing (i.e. the arc burning voltage), one comes to the conclusion that the initial potential difference U between the plasma and the plate is about 40 V, which corresponds to an electron temperature in the helium background plasma of about 13 eV. It was assumed $T_e^{(He)} = T_i^{(He)} = 13\,\text{eV}$ in this work. The helium ions of the background plasma in these conditions are doubly ionized, so it is set $Z = 2$. The ionization energy E in equations (20) and (23) is set as 79 eV, which is the sum of the first and second ionization energies for helium.

The initial temperature of the plate is set to $T_0 = 1900\,\text{K}$, a value reported in [14] for the temperature of the plate immersed in the helium plasma before the laser irradiation. The background plasma electron density n_e in the expressions

Table 1. Sets of simulation conditions considered for the modeling of this work.

Simulation case	Plate radius R (mm)	Parameter a (mm)
1	100	0.4
2	10	0.1
3	10	0.4

for $j_i^{(\mathrm{He})}$ and $j_e^{(\mathrm{He})}$ was found by solving the equation $q_2 = q_4$ and turned out to be equal to $3.05 \times 10^{17}\ \mathrm{m}^{-3}$.

The laser pulse used to trigger the unipolar arc in the experiment [14] had a peak power of $10^{10}\ \mathrm{W\ m}^{-2}$ (which corresponds to that of ELMs expected in ITER) and a duration of ~0.6 ms. The impact site on the plate had a diameter of approximately 0.8 mm, when the the laser beam was normal to the plate. Accordingly, the parameters q_{peak} and τ in equations (25) and (26) are specified as $q_{\mathrm{peak}} = 10^{10}\ \mathrm{W\ m}^{-2}$, and $\tau = 0.3$ ms. The power of the laser beam is assumed to reach the maximum value at $t_0 = 5$ ms. Two values of the parameter a specifying the spatial variation of the external energy load are considered for simulations, $a = 0.1$ mm and $a = 0.4$ mm.

The plate thickness in the modeling is 0.2 mm; two values of the plate radius R have been considered for the modeling, namely $R = 10$ mm and $R = 100$ mm.

Note that some important experimental parameters are not reported in [14], e.g. the temperature of the helium ions. A value of 6 eV for the electron temperature in the background plasma, mentioned in [14], is difficult to reconcile with the reported measured initial potential difference (i.e. floating potential) of 60 V: an estimate obtained by means of the well-known formula for the determination of the floating potential gives an initial floating potential of approximately 21 V. Therefore, no attempt was made to perform simulations for exactly the same conditions as in [14]; the objective was rather to report illustrative results of modeling of the interaction of an external energy flux with and current transfer to a tungsten metal plate immersed in a helium background plasma.

3. Numerical results and discussion

Let us consider the results obtained by simulations in the framework of the model described above. Three sets of simulation conditions have been considered for the modeling of this section, with different values of the radius R of the tungsten plate and of the parameter a specifying the spatial variation of the external energy load, table 1.

3.1. Potential of the plate below the plasma potential

The computed temporal evolution of the temperature distribution in the metal plate and of the plate surface deformation is shown in figure 2 for the simulation case 1. Figure 3 depicts the temporal evolution of the potential difference U between the plasma and the plate and of relevant arc spot parameters, namely the maximum plate temperature T_{max}, the current I_1 transferred by the tungsten plasma in the spot, the maximum pressure exerted by the produced tungsten plasma $p_{1,\mathrm{max}}$, and the maximum velocity of the melt v_{max}, for case 1.

The external energy flux (laser beam) comes into play at, say, $t = 4.5$ ms (at this moment, $q_3 \approx 10\%\ q_{\mathrm{peak}}$). The maximum plate temperature starts rapidly increasing and at approximately 4.7 ms melting of the surface begins, figure 2(b). Simultaneously, the pressure exerted over the surface by the produced tungsten plasma grows, figure 3(c), and pushes the molten metal outwards; a crater begins forming at approximately 4.9 ms, figure 2(c). The surface temperature attains a maximum of about 5200 K when the power delivered by the external energy load is at maximum, which happens at 5 ms; figure 3(a). The potential difference between the plasma and the plate is reduced from the floating potential to approximately 18 V, figure 3(a), and the current transferred in the arc spot reaches a maximum of about 400 A, figure 3(b). The formed crater expands on the plate surface (states (c)–(e) in figure 2), achieving a final depth of approximately 50 μm and a radius of approximately 300 μm; figure 2(f). The maximum temperature decays quickly to a little less than 4000 K after the external irradiation has ceased at $t \approx 5.5$ ms, and then remains approximately constant for nearly 3 ms (until $t \approx 8.5$ ms), after which the temperature decay resumes. No jet formation, or droplet detachment occurs.

The computed temporal evolution of the potential difference U between the plasma and the plate and of relevant arc spot parameters for case 2 are shown in figure 4; for brevity, we skip the analog of figure 2 and note only that the crater dimensions are smaller than in the preceding case 1, due to the parameter a specifying the spatial variation of the external energy load being smaller as well.

The temporal evolution in case 2 occurs in essentially the same way as in case 1, and only the most relevant aspects are discussed here. Melting of the surface begins at 4.7 ms, and at 4.8 ms a crater begins forming. The surface temperature attains a maximum of about 5200 K, and the potential difference U is reduced to approximately 5 V; figure 4(a). The current transported by the tungsten plasma in the arc spot attains a maximum of about 17 A, figure 4(b). The temperature decays very quickly after the laser irradiation has ceased, and the final crater depth and radius are approximately 10 μm and 70 μm, respectively.

Let us now consider the above-described evolution in cases 1 and 2 in some detail. Fluxes of helium ions and electrons compensate each other at each point of the plate surface, before the external energy load (laser) starts acting; the potential difference between the plasma and the plate equals the floating potential, as shown by the horizontal section of the dependencies $U(t)$ in figures 3(a) and 4(a). The plate surface starts being subjected to the external energy load at approximately 4.5 ms, and the increase in the temperature results in the initiation of electron emission and vaporization of tungsten atoms with their subsequent ionization in the laser impact site, i.e. the ignition of an arc spot. The transfer of

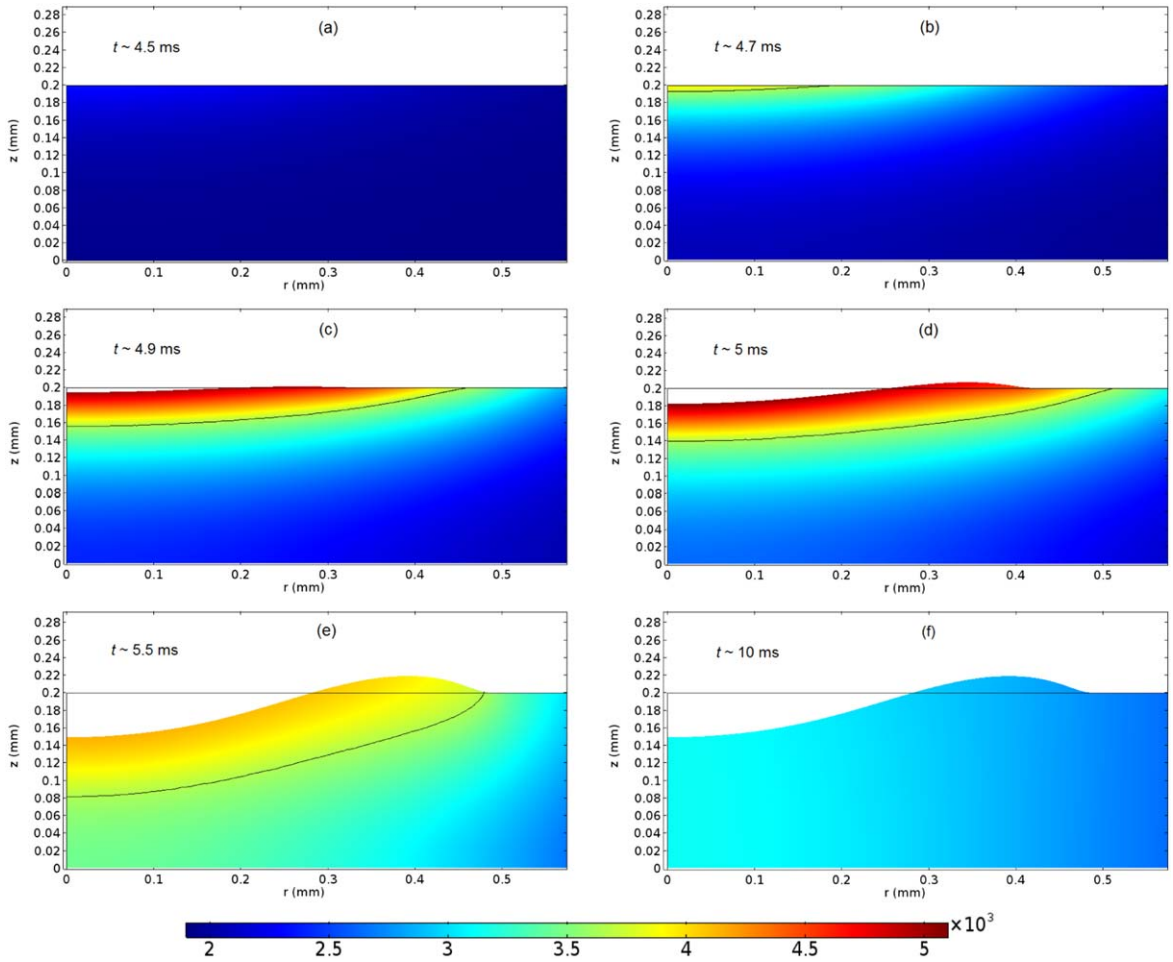

Figure 2. Evolution of the temperature distribution and plate surface deformation, in simulation case 1 ($R = 100$ mm and $a = 0.4$ mm). The bar in K. The black line represents the melting temperature isotherm.

current by the produced tungsten plasma is initiated. I_1, which initially was zero, starts rapidly increasing, figures 3(b) and 4(b), due to not only the continued increase in temperature, but also due to the expansion of the arc spot, which is shown in figures 2(b)–(d). Furthermore, as the production of the tungsten plasma increases and the ionized atoms return to the surface, the pressure exerted on the surface by these ions starts growing as well, figures 3(c) and 4(c), and pushes the molten material in the arc spot outward. A crater with a rim begins forming. Note that the highest values of the melt velocity (which reach about 1.8 m s^{-1} and 1.2 m s^{-1} in cases 1 and 2, respectively; see figures 3(c) and 4(c)) always appear at the surface at the crater periphery close to the rim, while most of the melt has significantly lower velocities below 0.5 m s^{-1}. Very little to no circulation of the flow is observed, i.e. the molten metal always flows away from the center toward the crater rim.

The ignition of the arc spot leads to a reduction of the potential difference U between the plasma and the plate, from the floating potential to the arc burning voltage of about 18 V in case 1 and 5 V in case 2; figures 3(a) and 4(a). This decrease allows a greater influx of electrons from the background plasma; the current transferred by the ions and the electrons of the helium plasma from the surface of the plate into the plasma increases so as to balance the current I_1 transferred in the arc spot. The potential difference U does not reduce further, i.e. no inversion of U occurs in either case, and the plate potential remains below the plasma potential at all stages of the simulation.

The arc spot starts cooling down after the external energy load is switched off, as heat is removed from the spot by electron emission and heat conduction into the plate, and the transfer of current in the spot rapidly decays, as well as the current transferred by the helium plasma. The crater expansion stops as the melt velocity quickly reduces to zero; figure 2(e). The potential difference between the plasma and the plate returns to the floating potential. In case 1, after an initial rapid decrease, the surface temperature remains more or less constant for some time at a level slightly below 4000 K, after which the plate cools down further. In case 2, the surface temperature decays very quickly, within 0.5 ms, to a level slightly above 2000 K, after which the plate cools down further at a slower rate. Note that the net current transferred to the plate is zero at all stages of the simulation, as is characteristic of the unipolar arc [7].

The model being used allows a self-consistent evaluation of the erosion of the tungsten plate, stemming from vaporization of the metal atoms in the arc spot (we remind that the simulations

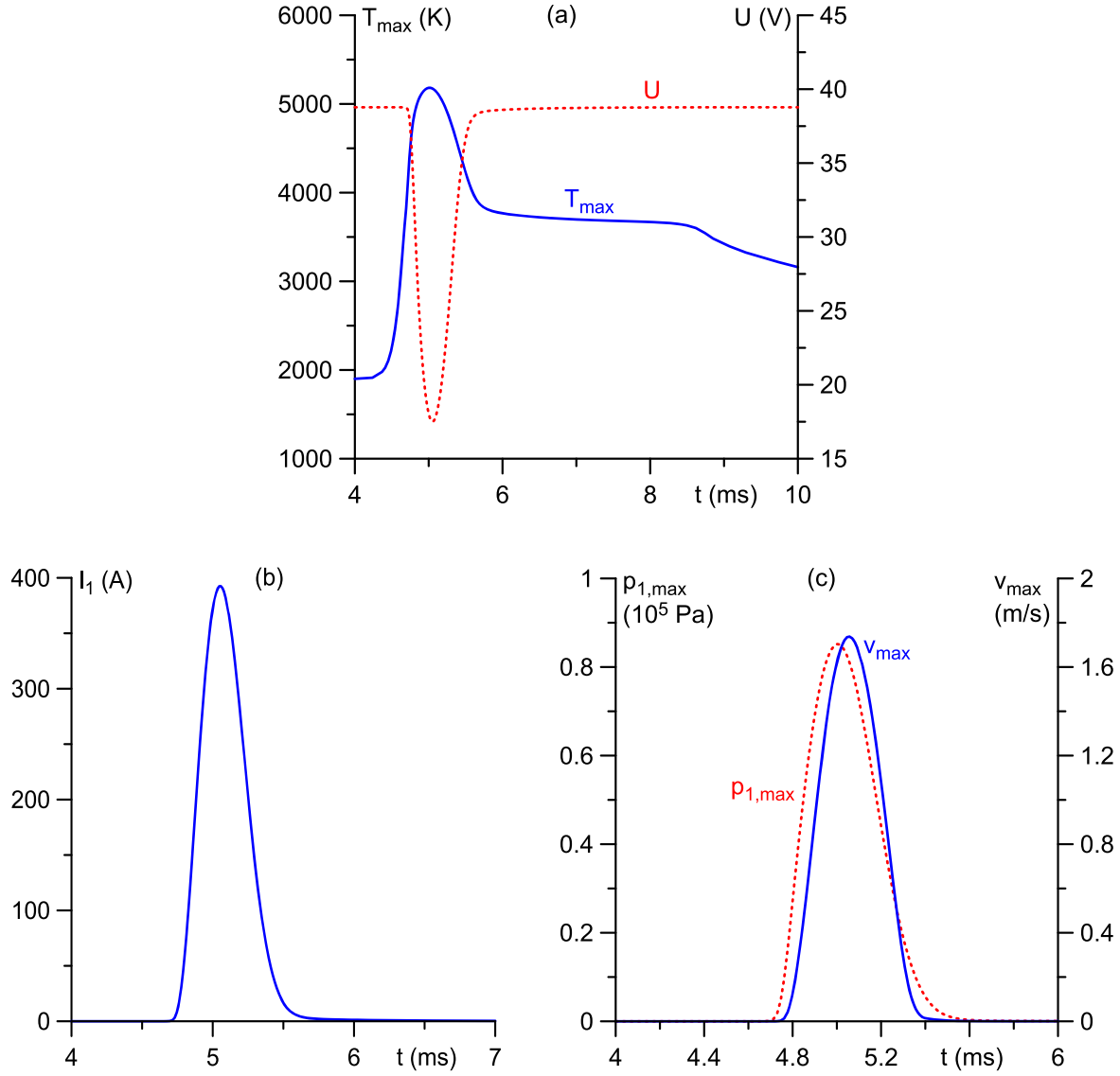

Figure 3. Results of simulation of the initial phase of unipolar arcing, in simulation case 1 ($R = 100$ mm and $a = 0.4$ mm).

of this work have revealed the formation of a crater, but no jet formation or droplet detachment). The total mass of vapor emitted from the arc spot during its lifetime is evaluated as $\Gamma_v^{(W)} = \int\int m_i^{(W)} J_v \, dA \, dt$, where the integrals are evaluated over the face of the plate subjected to the external energy load and over the lifetime of the arc spot. For cases 1 and 2, the computed values of $\Gamma_v^{(W)}$ are, respectively, 1.4 and 0.066 μg; the latter values differ between the two cases because the parameter a governing the arc spot size is different in cases 1 and 2.

The temporal evolution of the components of the density of the energy flux delivered to the plate surface (see equation (4)) at the center of the arc spot is shown in figure 5(a) for simulation case 1 and figure 5(b) for simulation case 2. The component q_1 is negative at each moment of the simulation, since the electron emission cooling exceeds heating by the ions and electrons produced by ionization of the tungsten vapor emitted in the spot; a more detailed discussion is given in section 4.1 below. One can see that the energy balance of the spot is dominated by the external energy load (q_3) and electron emission cooling ($-q_1$), the energy flux delivered to the plate by the ions and the electrons from the background helium plasma (q_2) and the radiation cooling (q_4) are minor effects.

Evolution of T_w at the center of the arc spot is virtually the same up to $t = 5$ ms in cases 1 and 2, while the difference in U is more pronounced (the minimum values of U attained in each simulation are 18 V and 5 V, respectively). The fact that there is little difference in the maximum values of ($-q_1$) seen in figure 5 shows that a significant difference in the value of the potential difference U at the same temperature T_w (as is the case in simulation cases 1 and 2) only slightly affects the electron emission cooling. The effect of U on the energy flux q_2 delivered to the plate by the background helium plasma is greater, as seen in figure 5, but, as mentioned above, q_2 is negligible inside the arc spot. Thus the variation of the potential difference U between the plasma and the plate plays only a small role in the energy balance of the spot.

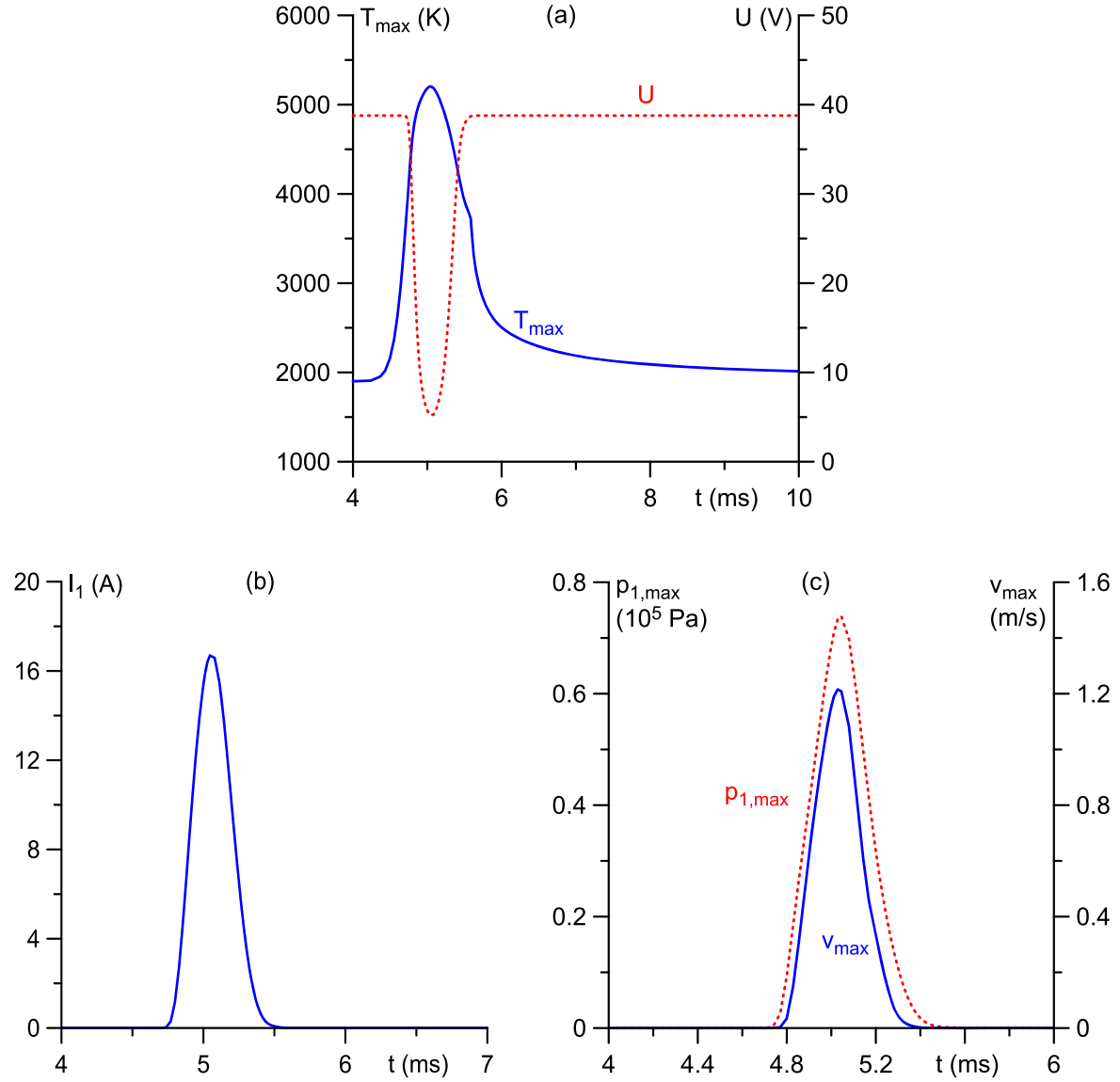

Figure 4. Results of simulation of the initial phase of unipolar arcing in simulation case 2 ($R = 10$ mm and $a = 0.1$ mm).

Note that another simulation was performed for case 2, where the helium ions were assumed to be singly ionized and the ion temperature $T_i^{(\mathrm{He})}$ was close to the room temperature (i.e. $T_e^{(\mathrm{He})} \gg T_i^{(\mathrm{He})}$) and was thus neglected, i.e. parameters of the background plasma presumably closer to those of experiment [14]. The results do not differ greatly from those reported above: the maximum surface temperature attained was about 5100 K (rather than 5200 K) and the potential difference U was reduced to approximately 10 V (rather than 5 V). The different values are explained by slight changes in expressions (19) and (20), which mean that the current transferred by the helium plasma necessary to compensate I_1 of figure 4(b) is obtained at a higher value of U than in the first simulation in case 2.

3.2. Potential of the plate above the plasma potential

The third simulation case, the one with a plate radius R of 10 mm and the spatial variation a of the external energy load equal to 0.4 mm, is the most similar to conditions of the experiment [14]. The temporal evolution of the temperature field and of the deformation of the molten surface in case 3 is qualitatively similar to those of the previous simulations, which is exemplified by figure 2. The crater dimensions are virtually the same as those resulting from case 1, with a depth of approximately 50 μm and a radius of about 300 μm. The computed temporal evolution of the potential difference U between the plasma and the plate and relevant arc spot parameters for case 3 are shown in figure 6. The most notable differences between the results of this and of the previous simulations are the potential difference U turning negative; a higher value of the temperature, which is approximately 7500 K; and a circulation of the melt on the periphery of the melted pool, which develops at $t \approx 4.9$ ms and is revealed by the change in sign of the radial component of the melt velocity v_r, as seen in figure 6(c).

U turning negative means that, as the laser heat load comes into play, the plate potential approaches that of the

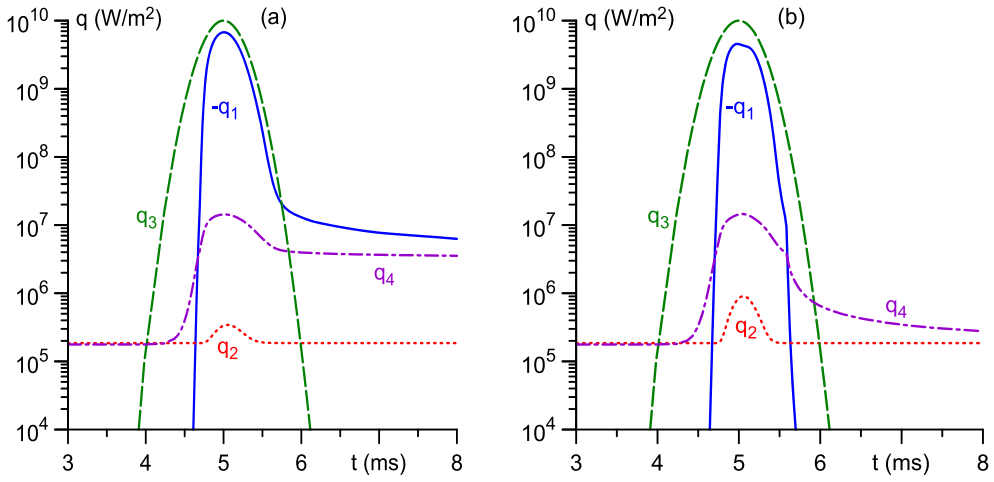

Figure 5. Temporal evolution of the components of the density of the energy flux q delivered to the plate surface in simulation case 1 (a) and 2 (b). q_1: density of the energy flux due to the tungsten vapor emitted in the spot, ions and electrons produced by ionization of the vapor, and the electron emission from the metal surface. q_2: density of the energy flux delivered to the plate by the ions and the electrons from the background helium plasma. q_3: density of the energy flux delivered to the surface by the external energy load. q_4: density of the energy flux lost by the plate surface due to radiation into the plasma.

plasma and then exceeds it, so a transition of the plate potential from below to above the potential of the plasma occurs at approximately 4.8 ms. The reason for this is as follows. The parameter a governing the arc spot (i.e. the laser impact site) size is the same in cases 1 and 3. The plate radius in case 3 is much smaller than that of case 1, the consequence being that there is a significantly lower current available from the helium plasma (see equation (6)) to balance the current transferred in the arc spot. Therefore, high values of the arc spot current I_1, which reach a few hundred amps in case 1, cannot be compensated in case 3 by the helium plasma current. Hence, the current I_1 transferred in the arc spot should be limited in case 3, and this is why the potential difference U between the plasma and the plate turns negative.

The regime with the plate potential above the plasma potential lasts a little less than a millisecond: a peak value of the plate potential of 3 V above the plasma potential (i.e. $U = -3$ V) is attained at $t = 5.1$ ms, i.e. very shortly after the maximum of the external energy load. After this, U begins increasing rapidly until becoming positive once more at 5.6 ms; figure 6(a). Subsequently, the potential difference between the plasma and the plate continues to rapidly increase until about 7 ms; after, the increase proceeds at a slower rate until U returns to the floating potential. The current I_1 transferred by the tungsten plasma in the spot attains a maximum of about 50 A at $t = 5.1$ ms, i.e. simultaneously with the maximum of the plate potential, figure 6(b).

An important result of the simulation of this section is the peak value of the temperature of the plate of 7500 K that is attained, which is higher by over 2000 K than the peak value obtained in the previous simulations. The higher peak temperature is owed to the reduction of the electron emission from the plate surface due to the transition to the regime with the plate potential above the plasma potential. In this regime, the emission of electrons is limited by the potential barrier (see equation (21)), which reflects the emitted electrons back to the surface, and thus significantly reduces the cooling due to electron emission, the dominant surface cooling mechanism. As a consequence, heating of the plate by the external energy source grows unhindered by any significant cooling, leading to a peak temperature higher than in the previous simulations, as well as to a higher value of the plate erosion, $\Gamma_v^{(\mathrm{W})} = 37\ \mu$g.

Figure 6(c) shows the distribution of radial velocity of the melt at $t \approx 5$ ms at three different radial positions on the plate, $r = 0.15$, 0.25, and 0.35 mm. Note that $z = 0.2$ mm corresponds to the plate surface, and the melting-point isotherm is positioned at $z \approx 0.13$, 0.14, and 0.16 mm for the three above-cited values of r, respectively. The solid and dashed lines of figure 6(c) show that in the central part of the melted pool the melt flows from the center of the pool towards its periphery and the velocity monotonically increases toward the surface and with increasing radial distance. On the other hand, at a position of $r = 0.35$ mm corresponding to the developing crater rim, v_r is negative in the range $0.16\ \mathrm{mm} \leqslant z \lesssim 0.195$ mm and turns positive at $z \gtrsim 0.195$ mm, i.e. very near to the surface, as shown by the dotted line on figure 6(c). In other words, the bulk of the molten metal at the pool edge flows back toward the center of the pool, with only a small part near the surface flowing outwards away from the center, resulting in a circulation of the melt at the pool periphery.

3.3. Effect of the nanostructure layer

In the experiment [14], the tungsten plate is initially exposed for 30 min to the helium plasma, the consequence of which is the formation of a fine layer of extremely thin nanostructures with a height of about 1.5 μm. The estimates cited in section 1 have shown that such nanostructures are rapidly destroyed when subjected to the laser energy load and can hardly affect the initial stage of unipolar arcing (in other words, the nanostructures within the laser impact site will have no effect on the ignition and development of the arc spot, as described

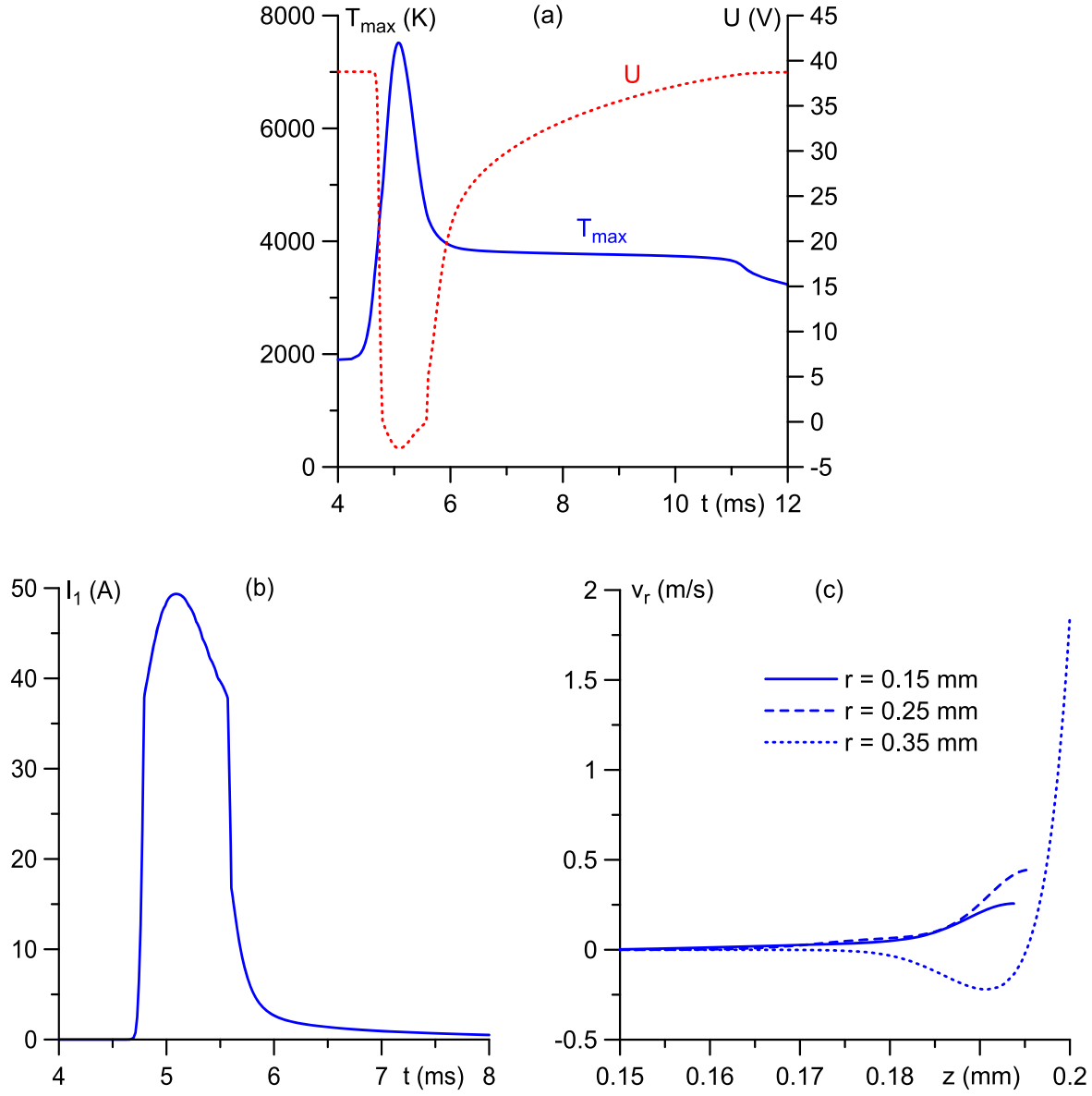

Figure 6. Results of simulation of the initial phase of unipolar arcing in simulation case 3 ($R = 10$ mm and $a = 0.4$ mm).

in more detail in section 1). In order to verify these estimates, special simulations have been undertaken.

A circular calculation domain representing the nanostructure layer is introduced directly above the (circular) tungsten plate, with the same radius and a height of 1.5 μm. The mass density and thermal conductivity of this layer are known to be significantly different from those of bulk tungsten; according to the experiments [32, 34], the mass density is reduced to approximately 10% of that of bulk tungsten, while the thermal conductivity becomes 1% or less of that of bulk tungsten. Thus, in the simulations reported in this section the (temperature dependent) mass density of the nanostructure layer is set to $\rho_{\text{layer}} = 0.1\rho$, and the thermal conductivity to $\kappa_{\text{layer}} = 0.01\kappa$ in the axial direction and to zero in the radial direction; here the mass density ρ and the thermal conductivity κ are those of the bulk tungsten. As the nanostructure layer is heated to the melting temperature T_{melt} and begins melting, the distinction between this layer and the bulk of the plate disappears; therefore, the above-mentioned values $\rho_{\text{layer}} = 0.1\rho$ and $\kappa_{\text{layer}} = 0.01\kappa$ are used for temperatures below T_{melt} and are replaced with the bulk values for $T > T_{\text{melt}}$. The other material properties (specific heat, viscosity and surface tension coefficient) remain unchanged, as well as all other parameters and material functions described in section 2.

Results of simulations performed with the account of the nanostructure layer in simulation case 1 are shown in figure 7. Figures 7(a) and (b) show the central part of the calculation domain, $0 \leqslant r \leqslant 0.035$ mm, 0.19 mm $\leqslant z \leqslant 0.2015$ mm, at two different moments, $t = 4.5$ and 4.6 ms. The nanostructure layer is positioned in the region 0.2 mm $\leqslant z \leqslant 0.2015$ mm, the rest of the calculation domain is the bulk tungsten. The layer is visibly hotter than the bulk, which, of course, is due to the reduced thermal conductivity of the layer. At approximately 4.6 ms, points on the plate surface start reaching the melting temperature, the nanostructure layer starts being destroyed and the differences between the layer and the bulk

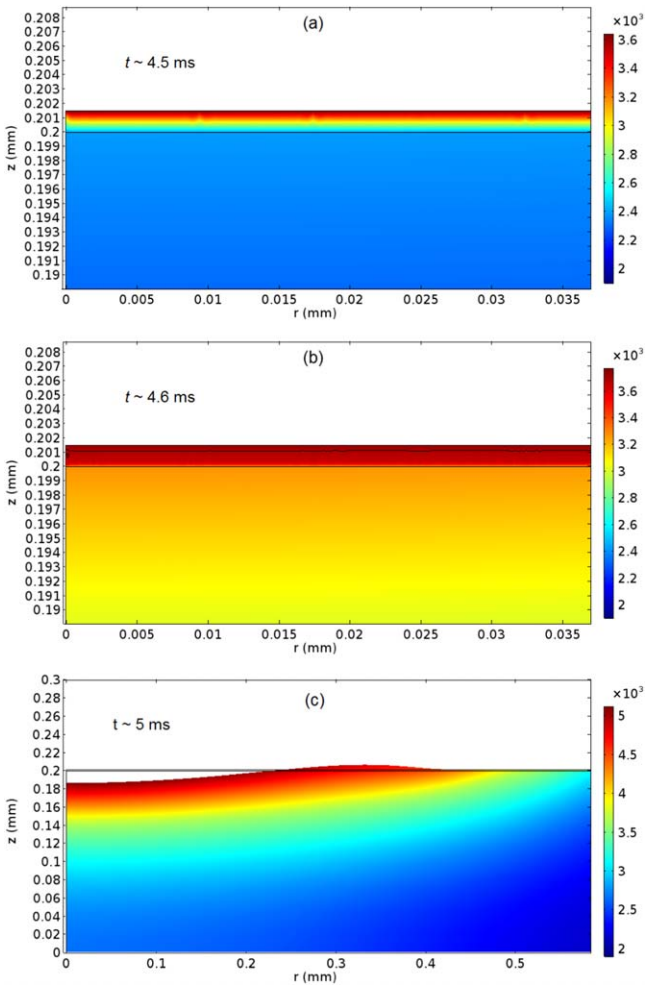

Figure 7. Evolution of the temperature distribution and plate surface deformation. The model takes into account the nanostructure layer. The bar is in *K*. (a), (b) The heated nanostructure layer is shown in detail. (c) Global overview of the forming crater.

tungsten plate disappear within a few microseconds. The nanostructure layer does not have an effect in the melting or deformation of the surface: figure 7(c) coincides with figure 2(d). Distributions at subsequent moments are also identical and skipped for brevity; in particular, the formed crater is identical to that in the modeling results shown in figure 2.

The dependence $T_{\max}(t)$ coincides with that from the modeling of section 3.1 except at the beginning, where the maximum plate temperature is slightly higher due to the reduced thermal conductivity of the layer; figure 8.

The simulations performed with the account of the nanostructure layer in the other simulation cases yield similar results. Thus, the effect of the nanostructure layer is negligible due to the rapid destruction of the layer, in agreement with the estimates in section 1, and the neglect of the nanostructures in the modeling of the initial stage of unipolar arcing is justified.

It should be stressed that this conclusion refers only to the initial stage of unipolar arcing, i.e. the production of the plasma due to the rapid heating, by an external energy flux, of a significant part of the electrode surface (i.e. the arc spot)

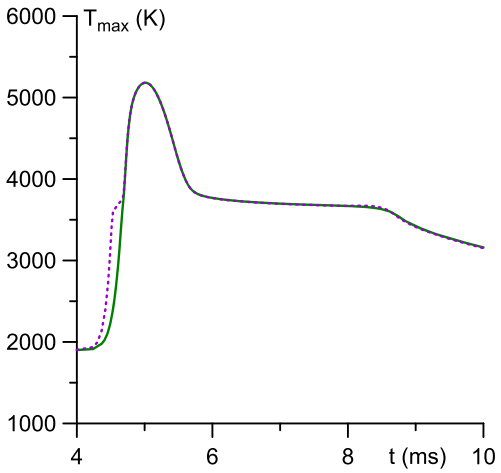

Figure 8. Temporal evolution of the maximum plate temperature in conditions of simulation 1. Dotted: model with account of the nanostructure layer. Solid: model without account of the nanostructure layer (from figure 3(a)).

which is much wider than individual nanostructures. The individual nanostructures presumably play a major role in the second phase of unipolar arcing, which occurs after the external energy flux is switched off, as discussed in section 1.

3.4. Parameters of the near-electrode plasma

It is of interest to consider parameters of the near-electrode plasma layer inside the arc spot. (We remind once again that the term 'arc spot' refers in the context of this work to the initial phase of unipolar arcing and means a wide heated area of the plate, i.e. the laser impact site, rather than the small bright spots responsible for current transfer at the second phase of arcing.) The thickness of the sheath at the center of the arc spot, i.e. of the sheath formed by the tungsten ions, $\delta^{(\mathrm{W})}$, evaluated by means of the Child–Langmuir sheath model in terms of the ion current density $j_i^{(\mathrm{W})}$ and U the potential difference between the surrounding plasma and the plate, is shown in figure 9 for $U = 20$ V as a function of the surface temperature T_w. Also shown is the characteristic distance of ionization $l_i^{(\mathrm{W})}$ of the evaporated tungsten atoms estimated in the framework of the model [60]. Note that, in the simulations of this work, the range of T_w relevant to the following discussion is $T_w \gtrsim 4500$ K, since this is the surface temperature at which current transfer by the tungsten plasma produced in the arc spot is initiated, i.e. the ignition of the arc spot occurs and plasma production in the spot begins.

On one hand the assumption of a 1D treatment of the quasi-stationary near-electrode layer inside the arc spot, used in the model of this work, requires that the sheath thickness $\delta^{(\mathrm{W})}$ and the characteristic distance of ionization $l_i^{(\mathrm{W})}$ be much smaller than the transversal dimensions (the arc spot radius and the spatial distribution of the external energy load). Given the representative values shown in figure 9, these requirements are met with a sufficient margin in the range $T_w \gtrsim 4500$ K. (Note that for T_w below 4500 K, the representative values of $\delta^{(\mathrm{W})}$ and $l_i^{(\mathrm{W})}$ approach the same order of

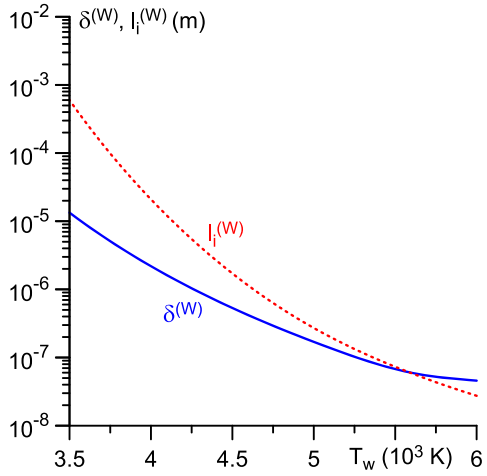

Figure 9. Parameters of the near-electrode plasma layer inside the arc spot. $\delta^{(W)}$: thickness of the sheath formed by the tungsten ions. $l_i^{(W)}$: characteristic distance of ionization of the evaporated tungsten atoms.

magnitude of the transversal dimensions, however no production of tungsten plasma occurs since the arc spot has not yet been ignited, or will have been extinguished after the laser irradiation has ceased.)

On the other hand, the above parameters are also useful in analyzing the potential effect of a magnetic field on the ions in the near-electrode layers. Assuming a magnetic field of 0.1 T as in the experiment [14], one finds that the Larmor radius of the ions produced from the ionization of the emitted tungsten vapor, $r_L^{(W)}$, is about 20 mm. One can see from figure 9 that $r_L^{(W)} \gg \delta^{(W)}$, $l_i^{(W)}$. The estimated sheath thickness due to the background helium ions, $\delta^{(He)}$, is approximately 95 μm, which is a few orders of magnitude smaller than the corresponding Larmor radius, $r_L^{(He)}$, which is about 7 mm. One can conclude that the effect of the magnetic field on the motion of the tungsten and helium ions in the sheath is negligible in the conditions [14] relevant for this work. Note that this is also the case in the conditions of cathodes of vacuum arcs [61].

In the operation conditions of fusion devices, the magnetic field is expected to be up to two orders of magnitude higher than that of experiment [14]. In such conditions, the estimated Larmor radii will be $r_L^{(W)} \sim 0.2$ mm and $r_L^{(He)} \sim 70$ μm. The former value will be still higher than $\delta^{(W)}$ and $l_i^{(W)}$ for $T_w \gtrsim 4500$ K, hence the effect of the magnetic field on the motion of the tungsten ions in the sheath inside the arc spot will still be negligible. On the other hand, $r_L^{(He)}$ will be lower than $\delta^{(He)}$, hence the magnetic field will affect the motion of the ions in the sheath outside the arc spot in fusion devices; a well-known effect.

4. Comparison with results for vacuum arcs

4.1. Parameters of plasma-metal interaction

An example of comparison of parameters of the tungsten plasma-metal interaction, described by the model of this work and by the model of near-cathode layers in vacuum arcs [62], is shown in figure 10 for two values of the potential difference between the surrounding plasma and the plate of $U = 20$ V and $U = 5$ V (i.e. in the regime with the plate potential being below the plasma potential) in the range of surface temperatures T_w relevant to the simulations of this work. Before proceeding to the comparison, let us briefly discuss general features of the results given by the model of this work, which are depicted in figure 10 by solid lines. For low local surface temperatures, the production of the vapor and its ionization are negligible and q_1, j_1, and p_1 are virtually zero. A significant tungsten plasma production starts as the temperature increases up to approximately 4000 K and $(-q_1)$, j_1, and p_1 rapidly grow. The behavior of parameters q_1, j_1 and p_1 for $U = 20$ V and $U = 5$ V is similar, with the computed values of $(-q_1)$, j_1, and p_1 being understandably lower for the smaller value of U. It is interesting to note that the density of the energy flux q_1 is negative in the whole range of temperatures shown, figure 10(a). The reason is that as the surface temperature increases, so does the emission of electrons from the surface; in fact, the cooling due to electron emission increases much faster than the heating due to ion bombardment, which means that the production of the tungsten plasma contributes to the cooling of the plate surface against the intense heating due to the external energy load.

The density of electron emission current is the dominant contribution to the density of electric current j_1 transferred in the spot, which reaches values of the order of 10^9 A m^{-2} at $T_w = 5000$ K, figure 10(b); the current transported by the tungsten ions returning to the plate is small. On the other hand, the pressure exerted on the plate due to ion bombardment is appreciable, of the order of 0.5–1 atm as seen in figure 10(c), and is sufficient to push the molten metal in the spot outward as discussed in section 3.

The dotted lines in figure 10 show the results of evaluation by means of the model of near-cathode layers in vacuum arcs [62], based on numerical modeling of the near-cathode space-charge sheath with ionization of atoms vaporized from the cathode surface [63], and employed in [40, 43]. Differences between the solid and dotted curves are minor for the case $U = 20$ V and become more pronounced for $U = 5$ V. The differences can be understood as follows. The model of near-cathode space-charge sheaths [51], used in this work, takes into account the limitation of the thermionic electron emission current by the emitted electrons accumulated in the sheath, while the model [63] does not. This results in lower values of the electron emission current density j_{em} and, consequently, of j_1 and q_1 given by the model of this work. The evaluation of the pressure p_1 exerted by the ion bombardment on the metal surface is also performed with different approaches in the two models, the one used in this work (equation (18)) being a more simplified approach than that of the model [62, 63].

It is of interest to compare the above parameters of the near-electrode layer on the tungsten plate with parameters of near-cathode layers on copper cathodes in vacuum arcs, evaluated in [62]. The density of energy flux q_1 in the latter case is positive for surface temperatures up to approximately

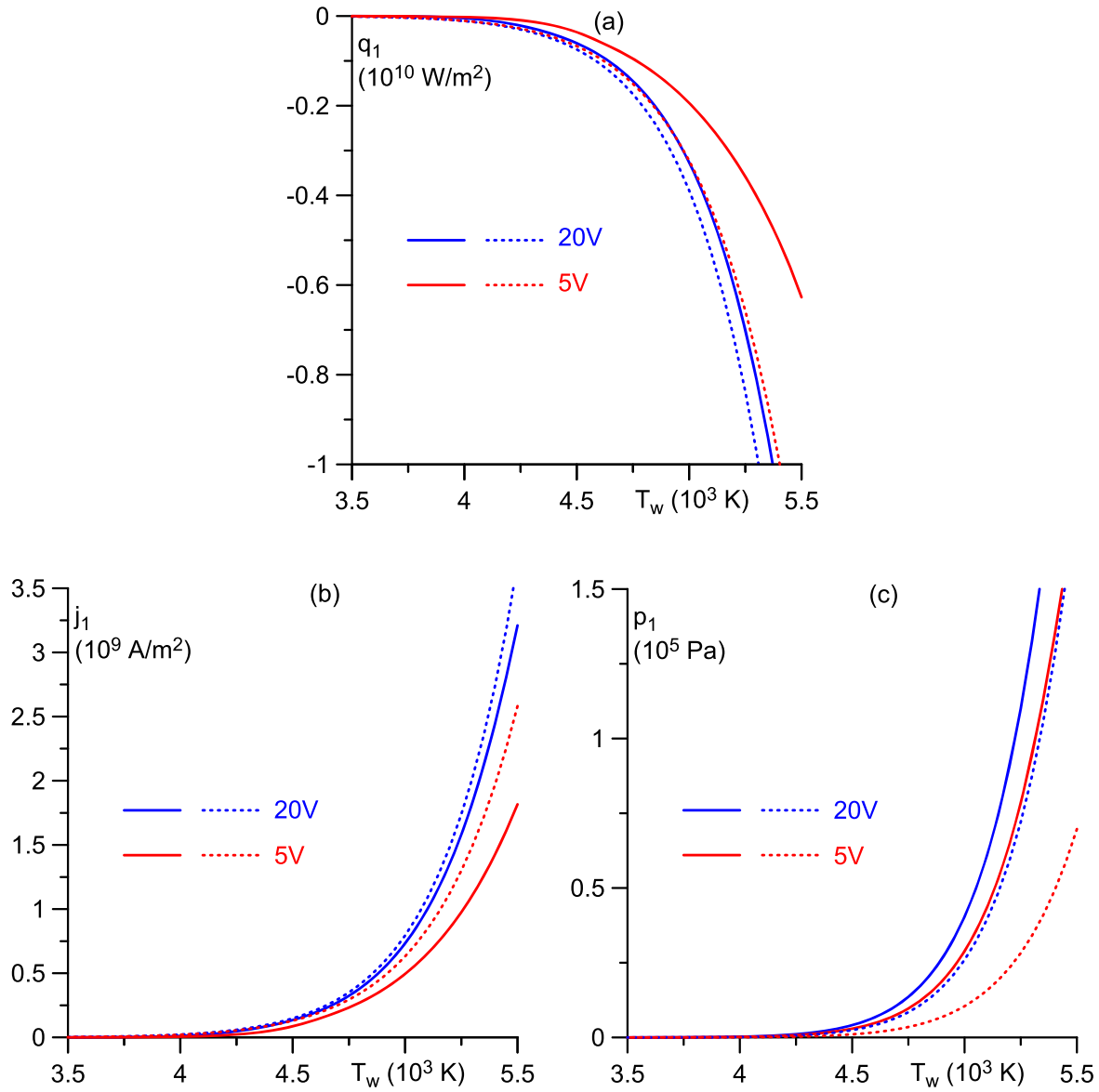

Figure 10. Computed values of q_1, j_1 and p_1. Solid: model of this work. Dotted: the model of near-cathode layers in vacuum arcs [62].

4300 K, since the ion heating exceeds the electron emission cooling, and is greater by up to 2 orders of magnitude; the density of electric current j_1 transferred in the spot and the pressure p_1 exerted by the plasma on the surface are up to 3 orders of magnitude higher. This difference arises due to the different natures of the two metals: copper is a volatile metal, while tungsten is a refractory metal with a significantly higher energy of vaporization. The latter, in particular, leads to an increase of the temperature at which the metal starts being vaporized and ionized in the spot.

4.2. Spot characteristics

It is of interest to compare characteristics of arc spots computed in this work with characteristics of spots on copper cathodes of vacuum arcs, computed in [40]. The pressure due to the tungsten ions returning to the surface is up to 4 orders of magnitude lower than the ion pressure in the modeling of vacuum arcs, which was up to 0.38 GPa. This explains why the velocities computed in the modeling of this work and seen in figures 3(c) and 4(c) are significantly smaller than the velocity of up to 180 m s^{-1} in the modeling of vacuum arcs (see figure 8(b) in [40]). As a consequence, the velocity acquired by the molten metal in the modeling of this work is insufficient to drive the formation of liquid-metal jets at the crater periphery.

The plateau in the temporal evolution of the maximum temperature, seen in figures 3(a) and 6(a), is seemingly similar to the plateau in the modeling of cathode spots in vacuum arcs reported in [40, 43], which is also a feature known from the modeling of cathode spots in arcs in high-pressure ambient gases [64]. However, the physics responsible for the plateau in the modeling of this work is different. In [40, 43], the plateau is owed to a balance between the heating due to ion bombardment and the cooling due to electron emission. In the modeling of this work, quantity q_1 is

negative in the whole range of the temperatures in the plate, which means that electron emission cooling is always greater than the heating due to ion bombardment. When the external energy load is switched off, at first, there is a fast decrease of the surface temperature due to strong electron emission cooling. As T_{max} decreases, the cooling due to electron emission is reduced significantly. The plate continues to cool down due to heat conduction into the bulk, but since the latter is a less intense mechanism compared to the cooling due to electron emission, the plateau in the temporal evolution of the temperature appears, figures 3(a) and 6(a). Eventually, the melt solidifies completely; since the thermal conductivity of tungsten almost doubles at the solidification, the plate temperature continues decaying further at a faster rate.

The arc spot current I_1 computed in the different simulation cases studied in this work is larger than the current of spots on cathodes of vacuum arcs, while the current density j_1 is 2–3 orders of magnitude smaller. The reason is that the arc spot size is significantly larger in the initial phase of unipolar arcing. On the other hand, one could expect that the current of the much smaller spots ignited during the second phase of arcing would be much closer in value to that of the spots on cathodes of vacuum arcs.

Unipolar arcing is characterized by a zero net current transferred to the electrode at each moment, ensured by the balance between the current transferred in the arc spot and the current transferred by the background plasma outside the arc spot. Since this balance is to be maintained during the laser action, the potential difference U between the plasma and the electrode lowers and, in particular conditions, may become negative, which amounts to the potential of the plate surpassing the potential of the plasma. It should be stressed that the arc spot continues to operate as a cathode in this regime. On the other hand, the potential difference between the plasma and the cathode is always positive in cathode spots in vacuum arcs.

The erosion of the metal plate in the modeling of this work stems from vaporization of the metal atoms in the arc spot (no jet formation or droplet detachment occur), resulting in a loss of mass of the tungsten plate of up to a few tens of micrograms. In contrast, the dominant mechanism of erosion of copper cathodes of vacuum arcs is the ejection of liquid droplets, while the mass loss due to vaporization is negligible. It is also interesting to note that the erosion of the tungsten plate is much more significant than that of the copper cathodes of vacuum arcs, due to the heated area on the electrode (i.e. the arc spot size) being larger in the former case; to exemplify, the arc spot radius in the modeling of this work is approximately 400 μm, while in the modeling [40] it is about 5 μm.

5. Summary and concluding remarks

The results of experimental works on unipolar arcs [14, 19, 24–30] suggest that there are two phases of unipolar arcing. An intense external energy flux, i.e. the laser pulse, causes significant heating of a wide region of the plate surface and the potential difference between the plasma and the plate is reduced by some 30 V; the initial phase. After about 0.6 ms the laser beam is switched off, however the potential difference remains the same and small (much narrower than the laser impact site) bright spots are seen moving away from the impact site. This second phase of unipolar arcing lasts for about 3 ms. The authors of works [36, 37] assume explosions of the nanostructures, in agreement with the model [35], to be the arcing mechanism of both phases of unipolar arcs.

There is little doubt that explosions of the nanostructures, hypothesized by the authors [36, 37], may be the governing mechanism at the second phase of unipolar arcing. However, this is less certain as far as the initial phase is concerned. Order of magnitude estimates show that, at the laser impact site, a nanostructure with a height of the order of 1 μm, as those of the experiment [14], will be melted within one or few microseconds. Hence, the nanostructures can hardly affect the initial phase of unipolar arcing. A possible alternative mechanism is the same as that of the life cycle of cathode spots in vacuum arcs: at the heated laser impact site, significant vaporization and electron emission occur, the latter causing the ionization of the emitted vapor. Consequently, current transfer is initiated and the plate potential increases, so that the electron current outside of the laser impact site compensates the current transfer inside the site, i.e. unipolar arcing is triggered. In this sense, the laser pulse interaction with the surface represents the initial phase of unipolar arcing and the impact site can be called an arc spot.

A model for the initial phase of unipolar arcing has been developed on the basis of the detailed numerical model of plasma-cathode interaction in vacuum arcs [40]. The model takes into account an external heating which triggers the arc spot, the vaporization of the atoms from the heated surface, the ions and electrons produced by ionization of the vapor, the electron emission from the metal surface, and relevant hydrodynamic phenomena, including convection and surface deformation. Since the arc is unipolar, the model [40] is supplemented with an account of current transfer outside the arc spot and the potential difference between the plasma and the metal surface (the plate) is evaluated from the condition that the net current transferred to the plate is zero at each moment.

The developed model is used for simulation of the interaction of an external energy load (laser beam) with and current transfer to a tungsten plate immersed in a helium background plasma in conditions similar to those of the experiment [14]. Simulations were performed for different dimensions of the plate and laser beam radii. Note that no attempt was made to perform simulations for exactly the same conditions as in [14], rather, illustrative modeling results are reported.

An arc spot is ignited as the plate surface starts being subjected to the external energy load, and the potential difference U between the plasma and the plate is reduced from the floating potential to the arc burning voltage. After the external energy load is switched off, the arc spot is extinguished, and U returns to the floating potential. The results revealed the formation of a crater, but no jet formation or

droplet detachment. The latter is in contrast to what was found in the modeling of cathode spots in vacuum arcs [40] and is explained by significantly lower melt velocities in the conditions studied, when compared to those of cathode spots in vacuum arcs, which are much more extreme. It was found that the nanostructure layer has a negligible effect, due to its rapid destruction under the external energy load.

Of particular interest of the modeling conditions treated in this work are those with the spatial scale of variation of the external flux, a, equal to 0.4 mm; note that the laser beam radius in the experiments [14] was 0.4 mm. In the case where the plate is large ($R = 100$ mm), the peak temperature of the plate attained is 5200 K, the plate potential remains below the plasma potential at every moment, and no circulation of the melt is observed. In the case where the plate is small ($R = 10$ mm), a peak temperature of 7500 K is reached, the plate potential surpasses the potential of the plasma and remains above it for nearly a millisecond before returning to the floating potential, and circulation of the melt at the pool periphery occurs (the molten metal near the pool surface flows away from the center of the melt pool while the bulk of the melt near the pool edge flows toward the center of the pool).

The dominant mechanism of erosion in the initial phase of unipolar arcing is the vaporization of the metal atoms in the arc spot, in contrast to the case of cathode spots in vacuum arcs, where the ejection of droplets is the dominant mechanism of erosion, and mass loss due to vaporization is negligible. The amount of metal eroded during the event is 1.4 μg in the case where the plate is large and reaches a significantly higher value of 37 μg for the small plate.

Acknowledgments

The work was supported by FCT—Fundação para a Ciência e a Tecnologia of Portugal (the project Pest-OE/UID/FIS/50010/2019). The work at Universidade da Madeira was supported by the project PlasMa—M1420-01-0145-FEDER-000016, co-financed by the Operational Program of the Autonomous Region of Madeira 2014–2020.

ORCID iDs

H T C Kaufmann https://orcid.org/0000-0001-6740-2467
C Silva https://orcid.org/0000-0001-6348-0505
M S Benilov https://orcid.org/0000-0001-9059-1948

References

[1] Herrmann A, Balden M, Laux M, Krieger K, Müller H W, Pugno R and Rohde V 2009 *J. Nucl. Mater.* **390–391** 747
[2] Rohde V, Endstrasser N, Toussaint U V, Balden M, Lunt T, Neu R, Hakola A and Bucalossi J 2011 *J. Nucl. Mater.* **415** S46
[3] Rudakov D L, Chrobak C P, Doerner R P, Krasheninnikov S I, Moyer R A, Umstadter K R, Wampler W R and Wong C P C 2013 *J. Nucl. Mater.* **438** S805
[4] Rohde V and Balden M 2016 *Nucl. Mater. Energy* **9** 36
[5] Ohtsuka H, Maeno M, Suzuki N, Konoshima S, Yamamoto S and Ogiwara N 1982 *Nucl. Fusion* **22** 823
[6] Matthews G F *et al* 2016 *Phys. Scr.* **2016** 014070
[7] Robson A E and Thonemann P C 1959 *Proc. Phys. Soc.* **73** 508
[8] McCracken G M and Goodall D H J 1978 *Nucl. Fusion* **18** 537
[9] Maeno M, Ohtsuka H, Yamamoto S, Yamamoto T, Suzuki N, Fujisawa N and Ogiwara N 1980 *Nucl. Fusion* **20** 1415
[10] Behrisch R 1986 *Physics of Plasma-Wall Interactions in Controlled Fusion* (*NATO ASI Series, Series B: Physics*) (New York: Plenum) pp 495–513
[11] Pitts R A *et al* 2017 *Nucl. Mater. Energy* **12** 60
[12] Bazylev B N, Janeschitz G, Landman I S, Loarte A and Pestchanyi S E 2007 *J. Nucl. Mater.* **363–365** 1011
[13] Bazylev B *et al* 2008 *Fusion Eng. Des.* **83** 1077
[14] Kajita S, Takamura S and Ohno N 2009 *Nucl. Fusion* **49** 032002
[15] Miloshevsky G V and Hassanein A 2010 *Nucl. Fusion* **50** 115005
[16] Bazylev B, Igitkhanov Y, Coenen J W, Philipps V and Ueda Y 2011 *Phys. Scr.* **2011** 014054
[17] Coenen J W, Philipps V, Brezinsek S, Bazylev B, Kreter A, Hirai T, Laengner M, Tanabe T, Ueda Y, Samm U and The TEXTOR Team 2011 *Nucl. Fusion* **51** 083008
[18] Coenen J W *et al* (The TEXTOR-Team) 2011 *Nucl. Fusion* **51** 113020
[19] Kajita S, Fukumoto M, Tokitani M, Nakano T, Noiri Y, Ohno N, Masuzaki S, Takamura S, Yoshida N and Ueda Y 2013 *Nucl. Fusion* **53** 053013
[20] Makhlaj V A *et al* 2014 *Phys. Scr.* **2014** 014024
[21] Coenen J W *et al* (J-E Contributors) 2015 *Nucl. Fusion* **55** 023010
[22] Coenen J W *et al* 2015 *J. Nucl. Mater.* **463** 78
[23] Wiesen S, Groth M, Brezinsek S, Wischmeier M and J Contributors 2016 *Phys. Scr.* **2016** 014078
[24] Kajita S, Ohno N, Takamura S and Tsuji Y 2009 *Phys. Lett.* A **373** 4273
[25] Kajita S, Takamura S and Ohno N 2011 *Plasma Phys. Control. Fusion* **53** 074002
[26] Kajita S, Ohno N, Yoshida N, Yoshihara R and Takamura S 2012 *Plasma Phys. Control. Fusion* **54** 035009
[27] Kajita S, Hwangbo D, Ohno N, Tsventoukh M M and Barengolts S A 2014 *J. Appl. Phys.* **116** 233302
[28] Hwangbo D, Kajita S, Barengolts S A, Tsventoukh M M and Ohno N 2014 *Results Phys.* **4** 33
[29] Aussems D U B, Nishijima D, Brandt C, van der Meiden H J, Vilemova M, Matejicek J, Temmerman G D, Doerner R P and Cardozo N J L 2015 *J. Nucl. Mater.* **463** 303
[30] Barengolts S A, Tsventoukh M M, Kajita S, Hwangbo D and Ohno N 2016 *Proc. ISDEIV 2016 (Suzhou, China, 18–23 September 2016)*
[31] Baldwin M J and Doerner R P 2010 *J. Nucl. Mater.* **404** 165
[32] Nishijima D, Baldwin M J, Doerner R P and Yu J H 2011 *J. Nucl. Mater.* **415** S96
[33] Kajita S, Temmerman G D, Morgan T, van Eden S, de Kruif T and Ohno N 2014 *Nucl. Fusion* **54** 033005
[34] Kajita S, Yagi T, Kobayashi K, Tokitani M and Ohno N 2016 *Results Phys.* **6** 877
[35] Mesyats G A 1984 *J. Nucl. Mater.* **128–129** 618
[36] Barengolts S A, Mesyats G A and Tsventoukh M M 2010 *Nucl. Fusion* **50** 125004
[37] Barengolts S A, Mesyats G A and Tsventoukh M M 2011 *Proc. ICPIG 2011 (Belfast, Northern Ireland, 28 August–2 September)*
[38] Mesyats G A and Uimanov I V 2015 *IEEE Trans. Plasma Sci.* **43** 2241

[39] Mesyats G A and Uimanov I V 2017 *IEEE Trans. Plasma Sci.* **45** 2087
[40] Kaufmann H T C, Cunha M D, Benilov M S, Hartmann W and Wenzel N 2017 *J. Appl. Phys.* **122** 163303
[41] Zhang X, Wang L, Jia S and Shmelev D L 2017 *J. Phys. D: Appl. Phys.* **50** 455203
[42] Wang L, Zhang X, Wang Y, Yang Z and Jia S 2018 *Phys. Plasmas* **25** 043511
[43] Cunha M D, Kaufmann H T C, Benilov M S, Hartmann W and Wenzel N 2017 *IEEE Trans. Plasma Sci.* **45** 2060
[44] Benilov M S, Almeida N A, Baeva M, Cunha M D, Benilova L G and Uhrlandt D 2016 *J. Phys. D: Appl. Phys.* **49** 215201
[45] Voller V R and Prakash C 1987 *Int. J. Heat Mass Transfer* **30** 1709
[46] Brent A D, Voller V R and Reid K J 1988 *Numer. Heat Transfer* **13** 297
[47] Wuerz H, Pestchanyi S, Landman I, Bazylev B, Tolkach V and Kappler F 2001 *Fusion Sci. Technol.* **40** 191
[48] Wuerz H, Bazylev B, Landman I, Pestchanyi S and Safronov V 2002 *J. Nucl. Mater.* **307–311** 60
[49] Rozhanskij V A, Ushakov A A and Voskobojnikov S P 1996 *Nucl. Fusion* **36** 191
[50] Lewis R W and Ravindran K 2000 *Int. J. Numer. Meth. Eng.* **47** 29
[51] Prewett P D and Allen J E 1976 *Proc. R. Soc.* A **348** 435
[52] Anders A 2008 *Cathodic Arcs: From Fractal Spots to Energetic Condensation* (*Springer Series on Atomic, Optical, and Plasma Physics*) (New York: Springer)
[53] Benilov M S and Marotta A 1995 *J. Phys. D: Appl. Phys.* **28** 1869
[54] Scheiner B, Baalrud S D, Yee B T, Hopkins M M and Barnat E V 2015 *Phys. Plasmas* **22** 123520
[55] Tolias P 2017 *Nucl. Mater. Energy* **13** 42
[56] Yih S W H and Wang C T 1979 *Tungsten: Sources, Metallurgy, Properties, and Applications* (New York: Plenum Press)
[57] Lide D R 2003 *CRC Handbook of Chemistry and Physics* 84th edn (Boca Raton, FL: CRC Press)
[58] Gale W F and Totemeier T C (ed) 2004 *Smithells Metals Reference Book* 8th edn (Amsterdam and Boston: Elsevier Butterworth-Heinemann)
[59] Fortov V E, Iakubov I T and Khrapak A G 2007 *Physics of Strongly Coupled Plasma* (Oxford: Oxford University Press)
[60] Benilov M S 2010 *J. Phys. D: Appl. Phys.* **43** 175203
[61] Benilov M S, Kaufmann H T C, Hartmann W and Benilova L G 2019 *IEEE Trans. Plasma Sci.* pp 1–8
[62] Almeida N A, Benilov M S, Benilova L G, Hartmann W and Wenzel N 2013 *IEEE Trans. Plasma Sci.* **41** 1938
[63] Benilov M S and Benilova L G 2010 *J. Phys. D: Appl. Phys.* **43** 345204
[64] Benilov M S and Cunha M D 2003 *J. Phys. D: Appl. Phys.* **36** 603